Potential-enstrophy lengthscale for the turbulent/nonturbulent interface in stratified flow

Marco Boetti○
School of Mechanical Engineering, Tel Aviv University, Tel Aviv 69978, Israel

Maarten van Reeuwijk○
*Department of Civil and Environmental Engineering, Imperial College London,
London SW7 2AZ, United Kingdom*

Alexander Liberzon○
School of Mechanical Engineering, Tel Aviv University, Tel Aviv 69978, Israel

We study properties of the turbulent/nonturbulent interface (TNTI) between two layers of stratified fluids through direct numerical simulations (DNSs). Zero mean shear forcing creates moderate turbulence in one of the layers with the Taylor microscale Reynolds numbers in the mixed region of $\mathrm{Re}_\lambda = 35, 44$. We focus on the similarities and differences of the properties of stratified TNTIs due to two distinct types of forcing: (a) convection due to a boundary heat source and (b) agitation resembling a vertically oscillating grid experiment. Similarly to other stratified flows, the small scale dynamics of the TNTI in the present DNSs differ from what would be expected in comparable yet unstratified TNTIs. The interface cannot be indeed uniquely identified by the commonly used vorticity ω. Instead, the potential enstrophy Π^2 is shown to be the most appropriate marker in these flow cases. It is emphasized that the Kolmogorov lengthscale $\eta_K \sim \sqrt{\nu/\omega}$ is not representative of the small scale dynamics of the interface. Hence, an alternative lengthscale, η_Π, is defined, in analogy to the Kolmogorov scale, based on the potential enstrophy, $\eta_\Pi = (\nu^3/\Pi_*)^{1/6}$, being $\Pi_* = |g/\rho_0 \Pi|$. The conditionally averaged profiles of potential enstrophy Π^2, enstrophy ω^2, and turbulent kinetic energy dissipation ϵ of the two distinctly different turbulence forcing cases collapsed when scaled by η_Π at different time instants in each simulation. This implies not only the self-similarity of the small scale statistics of the TNTI in either of the two cases, but also the similarity between the statistics of the two different turbulent flows in the proximity of TNTI.

I. INTRODUCTION

Entrainment across turbulent/nonturbulent interfaces (TNTIs) in stratified fluids is important for a vast set of applications, such as the dynamics of the ocean, atmospheric pollution dispersion, and the spread of contaminants [1]. Entrainment is responsible for the mixing and exchange of mass, energy, momentum, and scalar quantities between the fluid regions [2,3].

In unstratified cases, the turbulent flow can propagate into the irrotational region, moving the TNTI by viscous action, defined by small Kolmogorov-sized scales [4,5]. The TNTI itself can be subdivided into viscous sublayer (VSL), as proposed in [4] with an estimated thickness of the order of the Kolmogorov lengthscale η_K, and turbulent sublayer (TSL) [5–7], depending on the relative magnitude of viscous diffusion and turbulent vorticity, ω.

The VSL is a result of the process by which vorticity diffuses into the quiescent region. The lengthscale associated with this phenomenon is controlled by the viscosity ν and the dissipation (the squared rate of strain), which is comparable in magnitude to enstrophy, ω^2. Therefore, the lengthscale, after appropriate dimensional analysis, could be $\sqrt{\nu/\omega}$, that corresponds to η_K up to a multiplicative factor of 2 [8–10]. The thickness of the TSL, responsible for the increase in vorticity between the viscous sublayer and a fully turbulent region, is defined as the thickness of the enstrophy jump. Results in [11–14] show that the turbulent sublayer thickness is of the order of magnitude of the Taylor lengthscale, λ. More recently, [15] demonstrated theoretically and experimentally that specifically in nonequilibrium turbulence the entrainment velocity scales with the Taylor velocity v_λ, rather than Kolmogorov velocity scale.

In general, the TNTI can be defined using the sharp change in magnitude of enstrophy, by a passive scalar or density and/or temperature [16,17]. Differences may arise in the interface identification by different markers [18]. This is explained by different governing processes near the TNTI: viscous diffusion versus molecular diffusion. The differences depend on the values of Prandtl or Schmidt numbers and for high Pr, Sc $\gg 1$ this may affect the statistics conditioned on the TNTI [19–21].

In stratified fluids the flow physics is more complex because turbulence is also responsible for the irreversible mixing of the entrained fluid that changes its properties [22,23]. Substantial insight into stratified mixing without mean shear was obtained in experiments that employed a vertically oscillating grid in a two-fluid layer system [24–26].

A characteristic feature of stably stratified fluids is the presence of internal waves that are triggered by the turbulent agitation and propagate through the fluid at angles that are determined by the local stratification. Researchers addressed the internal waves generated by the turbulent wake of a sphere moving horizontally in a linear stratification both experimentally [27,28] and numerically [29]. Internal waves due to turbulence mechanically activated by grids were studied in the laboratory and simulations in a linearly stratified fluid [30,31].

Internal waves in stratified fluids can produce vorticity in the previously quiescent zone [32]. Therefore, vorticity is not anymore a reliable marker of the turbulent/nonturbulent interface [19]. Therefore, in stratified turbulent flows, the potential vorticity $\Pi = \boldsymbol{\omega} \cdot \nabla \rho$ (where ρ is density), which is not transferred by the internal waves [33], was suggested to identify turbulent regions [31]. Even if its advantage in the study of the atmospheric convective boundary layer has been questioned [34], because the enstrophy varies several orders of magnitude between the turbulent side and the gravity waves in the free troposphere, Π has been successfully used to mark the nonturbulent and turbulent regions [31]. Potential enstrophy was also used in conjunction with enstrophy to identify TNTI in DNSs of turbulent stratified wake [19]. Recently Π was effectively used to detect the TNTI in shear-driven, linearly stratified, turbulent flow DNS [35]. The authors [35] performed in-depth analysis of ω and Π budgets, and estimated the interface thickness, studying flow properties near TNTI as the function of the buoyancy Reynolds number, $\mathrm{Re}_b = (L_O/\eta_K)^{4/3}$, which accounts for the effects of turbulence and buoyancy, where $L_O = \sqrt{\epsilon/N^3}$ is the Ozmidov lengthscale, and ϵ and N are the turbulent kinetic energy dissipation rate and buoyancy frequency, respectively.

One of the open questions with respect to the physics of the stratified fluids interfaces is whether a large-scale forcing on the turbulent side affects small-scale TNTI properties. We studied this aspect numerically through a comparative analysis of two stratified turbulent flows: one generated by a convective forcing through a boundary buoyancy flux, and another using a mechanical type of forcing, analogous to a vertically oscillating grid, both without mean shear.

We demonstrate that the statistics in the VSL scaled with the lengthscale η_k [4] has to be adjusted for the stratified turbulent cases, at least in the range of the Reynolds numbers of this work and for shearless forcing types we present. Another small-scale lengthscale, η_Π, defined with ν and Π, is developed. We then present the statistics scaled with η_Π, that show the small-scale self-similarity in the TNTI region for the two different flow cases, irrespective of their large-scale forcing type.

II. METHODS

Two cases with shearless turbulence are simulated: an oscillating grid turbulence case (hereafter denoted as G) and a convective boundary layer case (C). The direct numerical simulation is performed using the DNS code SPARKLE, which integrates the incompressible Navier-Stokes equations in the Boussinesq approximation [36,37]:

$$\frac{\partial u_i}{\partial t} + u_j \frac{\partial u_i}{\partial x_j} = -\frac{1}{\rho_0} \frac{\partial p}{\partial x_i} + \nu \frac{\partial^2 u_i}{\partial x_j^2} + b\delta_{i3}, \tag{1}$$

$$\frac{\partial b}{\partial t} + u_j \frac{\partial b}{\partial x_j} = \kappa \frac{\partial^2 b}{\partial x_j^2}, \tag{2}$$

$$\frac{\partial u_i}{\partial x_i} = 0, \tag{3}$$

where u_i is the velocity vector, $b = g(\rho_0 - \rho)/\rho_0$ is the buoyancy, ν is the kinematic viscosity and is κ the molecular diffusivity, g is the gravitational acceleration, and ρ_0 is a reference density. Equations (1)–(3) use Einstein notation, where $i = 1, 2$ represents the horizontal components, x, y, and $i = 3$ is the vertical direction, z. The code is fully parallelized, making use of domain decomposition in two directions. The spatial differential operators are discretized using second-order, symmetry-preserving central difference [38] and time integration is carried out with an adaptive second-order Adams-Bashforth method [36].

Both simulations have periodic boundary conditions applied at the lateral walls and free-slip conditions at the upper and bottom boundaries. At $t = 0$, the fluid is at rest and has a two-layer stratification with its interface at $z = h_0 \equiv h(t = 0)$. h corresponds to the mixing layer depth, described in Sec. II D. We choose ρ_0 to be the density of the bottom layer, which leads to $b_0 = 0$ for $z < h_0$ and $b_{\text{ref}} = \Delta b$ for $z > h_0$.

A. Grid turbulence simulation

The grid-generated turbulent flow (case G) is a DNS in a cuboidal domain of size $L_x \times L_y \times L_z = h_0 \times h_0 \times 2h_0$, on the $360 \times 360 \times 720$ mesh. The oscillating grid is implemented using a standard immersed boundary method, with a motion of the form

$$z_{\text{grid}}(t) = z_{\text{grid}_0} + 0.5S \sin(2\pi f t), \quad w_{\text{grid}} = 0.5S\, 2\pi f \cos(2\pi f t), \tag{4}$$

which is imposed by setting the velocity in the region occupied by the grid equal to $(0, 0, w_{\text{grid}})$; a qualitative representation of case G is shown in Fig. 1(a). To preserve the incompressibility of the fluid, the Poisson solver for pressure is called right after the computation of Eq. (4). Similar simulations with this forcing type were implemented several times in different contexts [39–41].

Key parameters of the oscillating grid case are the midstroke position of the grid, $z_{\text{grid}_0}/h_0 = -0.467$, the stroke length $S/h_0 = 0.267$, and the dimensionless oscillation frequency $f t^* = 42$, where $t^* = L/u'_{RMS}$ is the turnover time, u'_{RMS} the horizontal (longitudinal u' and transverse v') velocity fluctuations root mean square, and L is the integral lengthscale [42]. The thickness and the mesh size of the grid are $a/h_0 = 0.03$ and $M/h_0 = 0.2$, respectively. These were chosen to resemble an oscillating grid with solidity of 0.31, similar to the experiments performed in [43]. The parameters are set to develop a well-mixed turbulent layer in proximity of the initial buoyancy discontinuity located at h_0.

The Reynolds number is computed similarly to the experimental studies as $\text{Re} = u'_{RMS}L/\nu = K_g\beta_g/\nu$ [42,43], where K_g is the so-called grid action, and β_g is an empirical constant that depends on the grid characteristics S, f, M [44]. This approach is based on empirical relationships that define u'_{RMS} and L with the oscillating grid characteristics: $u'_{RMS} = K_g/d$, $L = \beta_g d$, where $d \equiv z - z_{\text{grid}_0}$ is the distance from the grid midstroke position. The results of the model [42] for K_g and β_g are shown in Figs. 1(b) and 1(c), respectively.
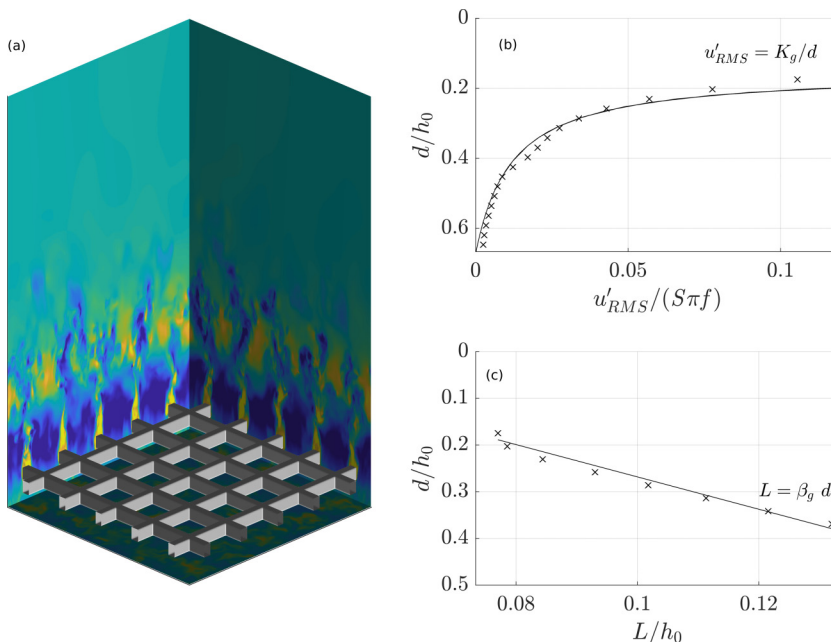
FIG. 1. Oscillating grid DNS case G: (a) Three-dimensional (3D) representation of the grid within the domain at $t/t^* = 3.8$; the colored fields represent the fluid vertical velocity. (b) Spatial distribution of u'_{RMS} and (c) longitudinal integral lengthscale as function of the distance from the grid, d.

B. Convective boundary layer simulation

The convective case (C) is simulated with a steady vertical heat flux $q_w = -\kappa \partial \theta / \partial z$ applied at the bottom boundary. The three-dimensional volume has $L_x \times L_y \times L_z = 4h_0 \times 4h_0 \times 2h_0$ size, with a computational resolution of $N_x \times N_y \times N_z = 720 \times 720 \times 360$. Similarly to G, this case also develops a fully mixed region between the turbulence source at the boundary and the initial density jump at h_0. In the case C the characteristic velocity of the convective mixed layer is $U = (\beta g q_w h_0)^{1/3}$ [45], with β the thermal expansion coefficient, and the characteristic lengthscale is $L = h_0$. The Reynolds number for the case C is $Re = UL/\nu = 1260$.

C. Further simulation details

Both simulations were performed for a period t_{run}, but all the results in Sec. III are computed after $t_{run}/2$ in order for the system to reach a quasistationary condition. Details are summarized in Table I. In addition to the domain sizes $N_{i=x,y,z}$, $L_{i=x,y,z}$ and the large-scale Reynolds number Re, Table I reports other key parameters: the Taylor microscale Reynolds number, $Re_\lambda = u_T \lambda / \nu$, and buoyancy Reynolds number, Re_b, which are more relevant for comparison of the well-mixed layers due to different large-scale forcing, and near the TNTI, respectively. Both parameters are given for two locations: at $z = h$, and closer to the turbulence source, in the well-mixed region, where stratification effect is negligible ($L_O \gg \eta_K$). Re_λ is computed using the Taylor microscales

TABLE I. The DNS cases main features.

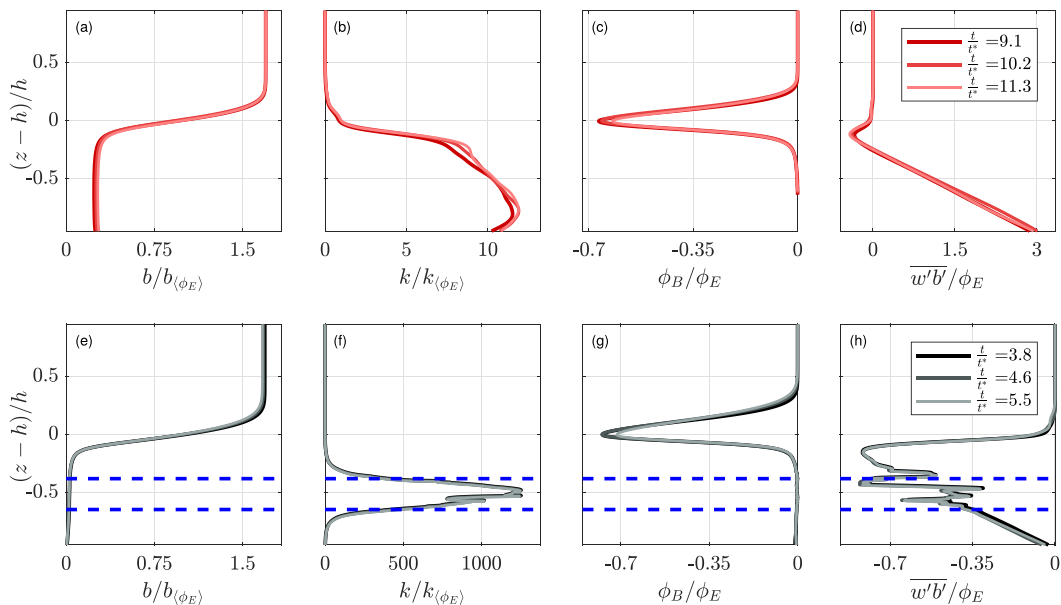|	$N_x\,N_y\,N_z$	$L_x\,L_y\,L_z/h_0^3$	Pr	Re	t_{run}/t^*	$Re_\lambda(z=h)$	$Re_\lambda(z=0.7h)$	$Re_b(z=h)$	$Re_b(z=0.7h)$	Ri	$\Delta z/\eta_K$
C	$720^2 \times 360$	$4^2 \times 2$	1.25	1260	16	13	44	0.210	105	240	0.91
G	$360^2 \times 720$	$1^2 \times 2$	1.25	92	6	8	35	0.125	21000	30	1.44

FIG. 2. Vertical profiles of case C (upper row), and case G (lower row) over time: (a, e) buoyancy; (b, f) turbulent kinetic energy; (c, g) diffusive flux; (d, h) turbulent flux.

$u_T \approx \sqrt{2k/3}$ and $\lambda = \sqrt{10\nu k/\epsilon}$, utilizing the turbulent dissipation rate, ϵ, and the turbulent kinetic energy $k = \frac{1}{2}(\overline{u'^2} + \overline{v'^2} + \overline{w'^2})$. The buoyancy Reynolds number Re_b, commonly representing turbulence intensity in stratified flows relates the influence of buoyancy and small-scale turbulence. The Ozmidov scale is computed with the frequency N defined as $(g\,d\bar{b}/dz)^{1/2}$. The strength of the stratification is estimated with the bulk Richardson number Ri. It is defined as $\mathrm{Ri} = \Delta b h / k$, where $k = k(z = 0.7h)$. The Prandtl number is set to $\mathrm{Pr} = 1.25$, for both cases G and C, to increase viscosity over molecular diffusivity.

D. Horizontally averaged statistics

Before presenting the conditional analysis, the basic statistics of the two cases are discussed. Figure 2 shows the spatial distributions of key flow properties of the two DNSs emphasizing their common features and differences. The horizontally averaged profiles of buoyancy b, turbulent kinetic energy k, the diffusive flux $\phi_B = -\kappa\,d\bar{b}/dz$, and the turbulent buoyancy flux $\overline{w'b'}$, are shown for the two DNSs (case C in the top row and case G in the bottom row). The quasistationary temporal evolution of these quantities is shown by color shades as explained in the legends. The profiles are horizontally averaged, with further averaging over one turnover time scale t^*. Since the emphasis of this paper is on the entrainment properties of different flows, the profiles are normalized by the value at the mixed layer depth h. The mixed layer depth h is diagnosed via the minimum of the diffusive buoyancy flux ϕ_B (or equivalently the inflection point of the mean buoyancy). b_{ϕ_E} and k_{ϕ_E} are then the buoyancy and the turbulent kinetic energy, sampled at $z = h$. The entrainment flux ϕ_E was determined following [46] by extrapolating the linear profile of the total buoyancy flux to the boundary layer depth h.

The horizontal dotted lines in case G [Figs. 2(e)–(h), at -0.6 and -0.33] mark the stroke of the grid. Since the fluid velocity in this region is directly affected by the oscillating grid motion, the corresponding volume is excluded from the conditional analysis in Sec. III B. The negligible differences between the curves with different shades, corresponding to the prescribed time intervals, emphasize that the systems have reached their quasi-steady-state regimes, for all the relevant

quantities. Moreover, Figs. 2(a) and 2(e) and Figs. 2(c) and 2(g) show that both simulation results have similar profiles for buoyancy and diffusive fluxes. This is one of the key similarity points of the two cases. It is also clear that, in the time needed to reach the quasisteady condition, the molecular diffusion causes the buoyancy profile to transition from the initial step function profile, with discontinuity at $z = h_0$, to a continuous profile with a transitional region at about $z \approx h$. The existence of this layer supports a region in which internal waves can propagate.

Despite the similarity in flux profiles, the two cases are different in their mechanisms: the convective C case produces turbulence via buoyancy $\overline{w'b'}$ over the entire mixed layer (apart from the entrainment zone in which $\overline{w'b'}$ is negative), while for the grid case G, the turbulence is generated at the grid and then transported through the mixed layer. Here, the buoyancy flux is negative throughout the mixed layer, which goes at the expense of the turbulence kinetic energy (TKE). This is evident in the profiles of turbulence kinetic energy, which are substantially different [Figs. 2(b) and 2(f)]. Figure 2(b) presents relatively large values of k throughout the bottom half of the domain before a sharp drop at $(z - h)/h < -0.2$. For the G case, Fig. 2(f), TKE decays with the reciprocal of the distance from the grid as $k^{1/2} \sim u'_{\text{RMS}} = K_g/(z - z_{\text{grid}_0})$ [42,47], right below the region of the direct agitation by the oscillating grid.

III. RESULTS

A. Definition of the turbulent/nonturbulent interface position

As mentioned in the introductory section, there are several possible definitions of TNTI. In unstratified cases, vorticity is used to separate rotational from irrotational fluid, based on either vorticity or enstrophy thresholds, $\omega^2 \geqslant \omega_{\text{th}}^2$. An appropriate threshold is chosen such that the conditional statistics near the TNTI do not significantly depend on its value (e.g., [5,8]). It is typically supported by the plot of the turbulent volume as a function of enstrophy, which exhibits a plateau at a properly chosen ω_{th}^2. It is also possible to visualize the interface position, its shape that should not vary strongly depending on the value of ω_{th}^2 (see, e.g., [6,48]).

In stratified cases, vorticity can be produced in the environment by internal waves [32,49]. This situation complicates the use of ω_{th}^2 as a TNTI marker. This may be especially relevant for low and moderate Reynolds numbers [34]. Conversely to ω^2, Π^2 is produced by viscous and diffusive effects [19]. Initially irrotational fluid regions may acquire potential enstrophy only by turbulence-related mechanisms (like entrainment) but not through internal waves.

Figures 3(a) and 3(b) and Figs. 3(d) and 3(e) show a two-dimensional (2D) vertical cross section (C and (G simulations, respectively), presenting the potential enstrophy [Figs. 3(a) and 3(d)] and enstrophy [Figs. 3(b) and 3(e)] with the former exhibiting a clear boundary between the turbulent and nonturbulent fluids. Note that the vertical axis is relative to the mixed layer depth h defined in the previous section, and it is clear that the instantaneous TNTI is situated about 20% higher than h. The instantaneous values of ω^2 can be seen to extend even further up, and are a result of the smooth stratification produced by molecular diffusion and to the relatively low values of Re which allow internal waves to propagate into this region. We experimented with a large number of indicators for TNTI, including enstrophy, and hybrid indicators [19], but in all other cases the results were unacceptably sensitive to the chosen threshold. Only potential enstrophy turns out to be a robust indicator for the TNTI, provided that the threshold is chosen sufficiently small. Figures 3(c)–(f) show the turbulent volume fraction V_T as a function of Π^2, normalized by its mean value $\langle \Pi^2 \rangle$ computed over the turbulent and quiescent regions (excluding the volume spanned by the oscillating grid in G). It is clear that V_T is only weakly dependent on the exact value near the chosen threshold: $4 \times 10^{-6} \langle \Pi^2 \rangle$ for case C DNS and $1.6 \times 10^{-6} \langle \Pi^2 \rangle$ for case G.

B. Comparison of the near-interface dynamics between the two cases

It is generally expected that the significant properties for the near-interface turbulent dynamics, driven by the viscous diffusion of vorticity into the irrotational region, are the kinematic viscosity
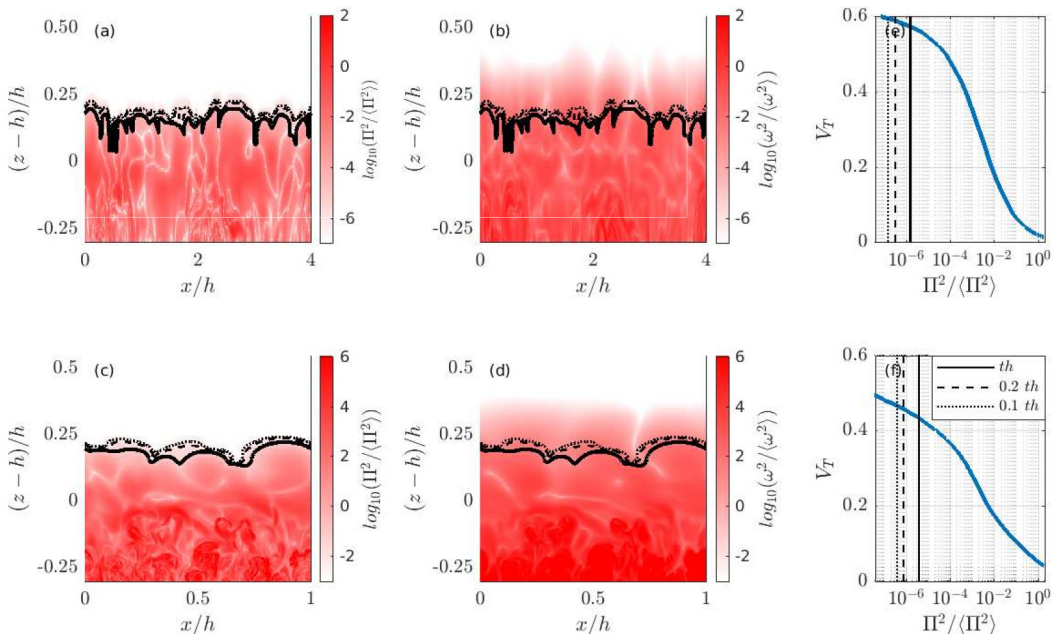
FIG. 3. Case C (upper row) and G (lower row): vertical cross section of (a–d) normalized Π^2, (b–e) normalized ω^2, and (c–f) turbulent volume fraction as function of Π^2. Black lines mark threshold (solid), 1/5 of threshold (dashed), 1/10 of threshold (dotted).

ν and vorticity ω [4,8,9]. The most relevant lengthscale in this region is the Kolmogorov scale, $\eta_K \sim \sqrt{\nu/\omega}$ (derivable from the more common expression $\eta_K = (\nu^3/\epsilon)^{1/4}$ using the relation $\varepsilon = 2\nu\omega^2$, valid in homogeneous isotropic turbulence [50,51]). Therefore, for the following comparison of the small-scale near-interface dynamics of the two DNS cases in Figs. 4 and 5 we normalize the distance to the interface, $z_* = z - z_I$, where z_I is the interface position, by η_K computed at the TNTI. We want to check if some similarities in the conditional profiles of Π^2, ω^2, k, and ϵ in Figs. 4(a), 4(c), 4(e), and 4(g) can be found. These quantities, scaled by η_K, do exhibit good self-similarity in time for each DNS separately. The conclusion one has to draw from these results is that the two simulations—despite both being driven by shearless turbulence—do not produce the same dynamics near the TNTI, with the turbulent quantities in C changing much more slowly as a function of z^*/η_K than G.

However, in the choice of the threshold indicator, it was quite clear that the enstrophy was not suitable for these cases. Since the potential enstrophy Π^2 was shown to be a robust TNTI indicator, it stands to reason to define a new local lengthscale

$$\eta_\Pi = \left(\frac{\nu^3}{\Pi_*}\right)^{1/6},$$ (5)

where Π_* is defined as

$$\Pi_* = |\overline{\omega} \cdot \nabla b| = \left| \frac{g}{\rho_0} \Pi_I \right|$$ (6)

and Π_I the square root of the threshold of potential enstrophy. η_Π defines the relevant scale in cases when the vorticity evolves not only through viscous diffusion, but also by stratification effects. In stratified cases Π^2 can only enter the nonturbulent region via molecular effects. Therefore,
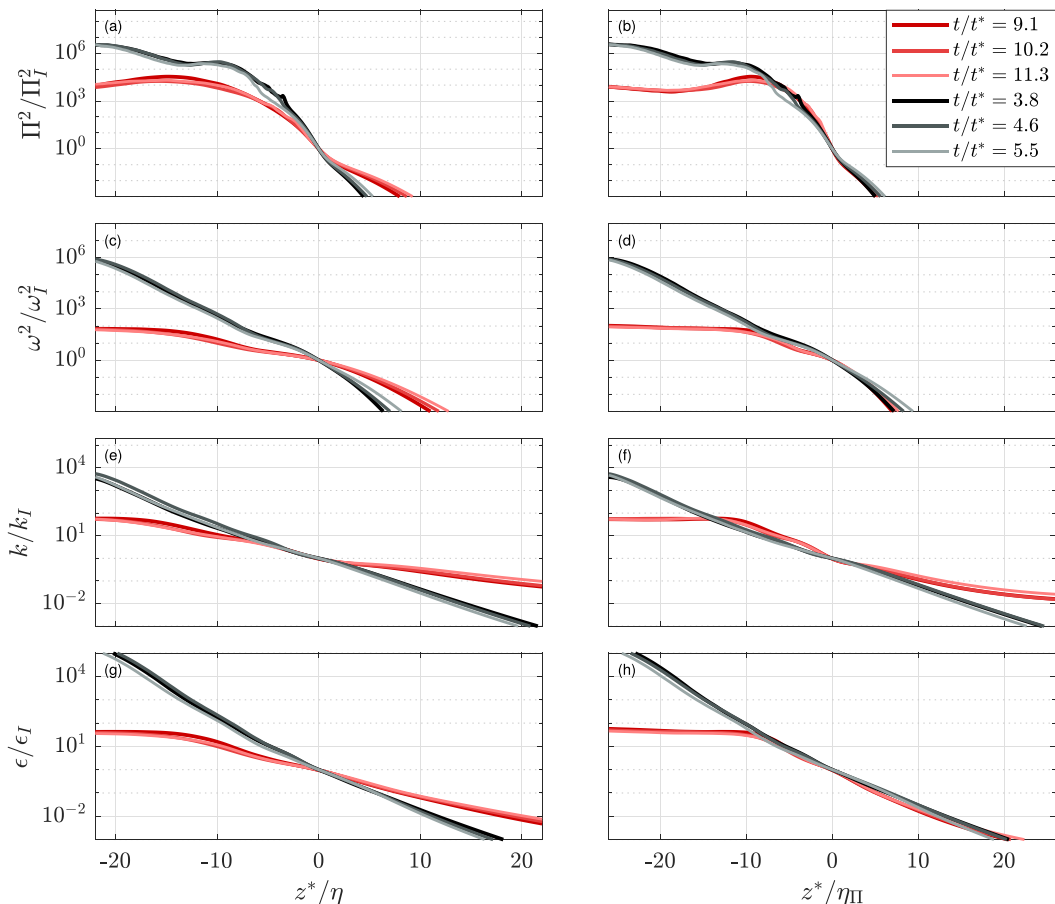
FIG. 4. Vertical conditional profiles of (a, b) Π^2, (c, d) ω^2, (e, f) k, (g, h) ϵ scaled with η_K (left column) and η_Π (right column). G, black curves; C, red curves.

applying a dimensional analysis using Π and ν to obtain a lengthscale, η_Π is the natural small-scale lengthscale.

The flow properties scaled with η_Π for both DNSs are reported in Figs. 4(b), 4(d), 4(f), and 4(h). The key result is that the two simulations exhibit remarkably similar behavior near the TNTI, when scaled based on η_Π. Indeed, for Π^2, ω^2, and ϵ, the profiles of \textrmG and \textrmC are nearly indistinguishable for $z^*/\eta_\Pi > -10$. Only the kinetic energy for the two cases deviates deeper into the nonturbulent layer ($z^*/\eta_\Pi > 5$).

Comparison of profiles of potential enstrophy and enstrophy in Figs. 4(b) and 4(d) further highlights the effectiveness of the proposed method for TNTI detection and the use of the new lengthscale. Not only does Π^2 present a larger magnitude in the "jump" across the interface as in [35], Π^2 curves also show a clear change in slope, with the presence of the inflection point at $z^* \approx 0$, and a distinct boundary between the turbulent and the nonturbulent regions which is sharper as compared to ω^2.

To provide a precise value for the TNTI thickness δ_I we followed the procedure proposed in [35] based on a fit of Gaussian shape to $\partial \Pi^2/\partial z$. This procedure yields $\delta_I \sim 10\eta_\Pi$ for both C and G. It is noteworthy that in the stratified shear driven flow [35] δ_I increased with decreasing Re_b, as the flow evolved in time. It remains to be studied whether this effect is present in shearless stratified cases on a larger range of Re_b.
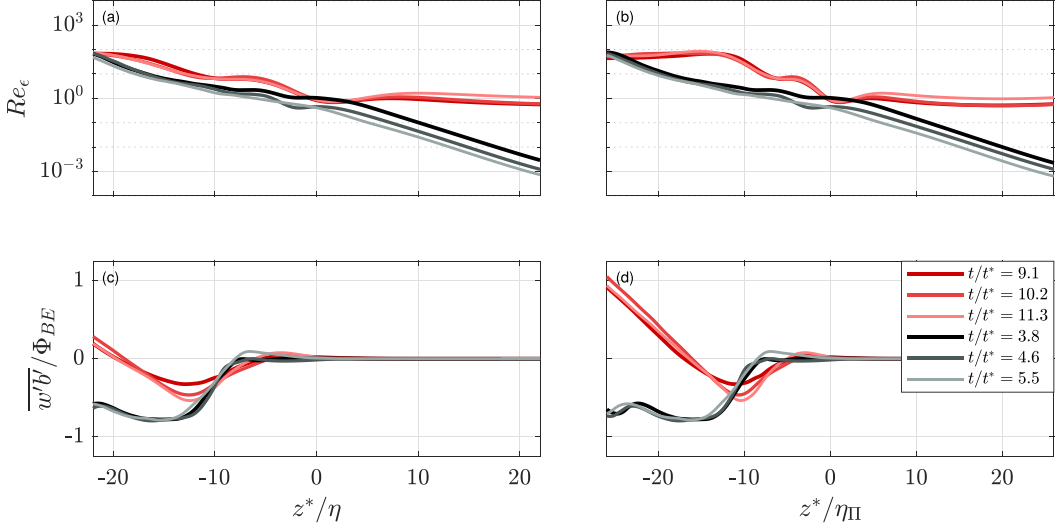
FIG. 5. Vertical conditional profiles of (a, b) Re_ϵ, (c, d) $\overline{w'b'}$ scaled with η_K (left column) and η_Π (right column). C, red curves; G, black curves.

We also computed the TNTI thickness with the Kolmogorov length η_K scaling: both DNSs present constant behavior in time; however, the difference in δ_I is larger between C and G than the results obtained from the η_Π. In case G $\delta_I = 10\eta_K$, while in C we obtain $\delta_I = 15\eta_K$. For completeness, we tested the viscous scale derived by [52] and used by [35] for low Re_b, but results were inconclusive.

We further compare the two cases and the scaling with the viscous lengthscale versus the new lengthscale in Fig. 5 presenting the turbulent Reynolds number $Re_\epsilon = k^2/(\nu\epsilon)$ and the turbulent buoyancy flux $\overline{w'b'}$. Here, no collapse is observed in either of the lengthscales. Both turbulence Reynolds numbers are $O(1)$ at the TNTI; the convective driven case C is more strongly agitated compared to the grid case G in the turbulent region, leading to higher values of Re_ϵ. This is possibly caused by the different nature of forcing type. The turbulent fluxes shown in Figs. 5(c) and 5(d) reflect, similarly to Re_ϵ, the different types of turbulent agitation of the two cases in the turbulent regions and the change from negative to positive values of $\overline{w'b'}$ that leads to a local maxima in the interfacial layer.

C. Vorticity structure in the near-TNTI region

One of the key questions is whether the vorticity dynamics is different between the two cases. We address this question by studying the alignment of vorticity vectors with the TNTI isosurface, conditionally sampled at different distances from the interface. The alignment of two three-dimensional vector fields can be characterized through the alignment angle θ, which is defined as $\cos\theta = \boldsymbol{\omega} \cdot \mathbf{n}/|\omega||\mathbf{n}|$, where $\mathbf{n}$ is the normal to the TNTI surface [53]. The alignment is analyzed through the conditional mean profiles and probability density functions (PDFs) of $\cos\theta$, in Fig. 6.

We observe a strong alignment between vorticity and the TNTI surface, similar to the results in [53]. This is expected at the TNTI interface, including stratified flow cases, since according to Helmholtz's second theorem a vortex filament either extends to the fluid boundaries or forms a closed path [54], hence vortical tubelike structures, associated to turbulence, could not end inside the fluid. Evidence for the above statement is shown in Fig. 6(a): a plateau at $-10 < z^*/\eta_\Pi$ where the minimum value of $\langle\cos\theta\rangle$ is approximately 0.3 for both DNSs.

The PDFs of $\cos\theta$ at three distance intervals are shown in Figs. 6(b), 6(c), and 6(e). The PDFs in the interval $[-20, -15]\eta_\Pi$ show that in the turbulent regions the vorticity angles are almost
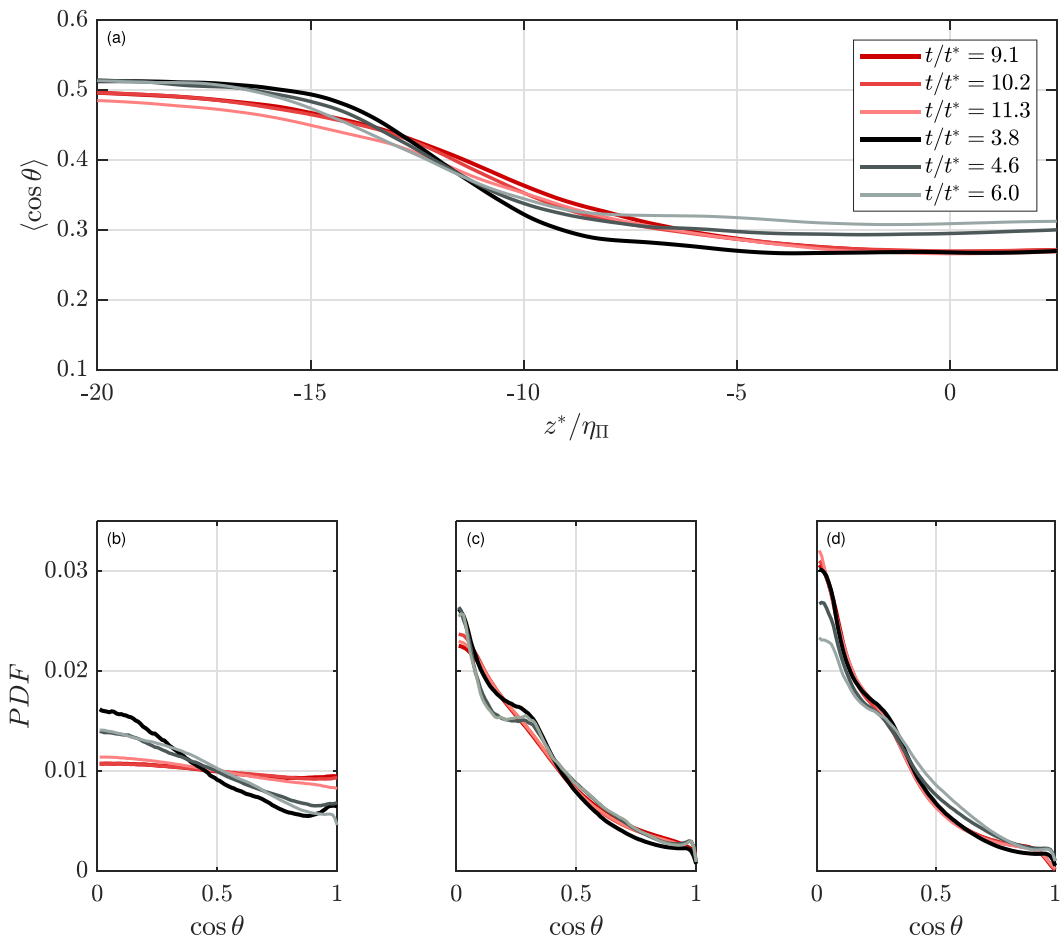
FIG. 6. Alignment of $\boldsymbol{\omega}$ with the TNTI normal $\mathbf{n}$. C, red curves; G, black curves. (a) Vertical profiles of $\langle \cos \theta \rangle$. PDFs of $\cos \theta$ at different interval height: (b) $-20 < z_I/\eta_\Pi < -15$, (c) $-10 < z_I/\eta_\Pi < -5$, and (d) $-2.5 < z_I/\eta_\Pi < 2.5$.

uniformly distributed and there is no preferential alignment. A lower Reynolds number in the G case compared to the C case is probably the reason for the small bias in the alignment. However, when getting closer to the TNTI, as in Figs. 6(c) and 6(d) that represent the intervals $[-10, -5]\eta_\Pi$ and $[-2.5, 2.5]\eta_\Pi$, respectively, we observe that the most frequent angle between ω and $\mathbf{n}$ is $\cos \theta = 0$ similarly to [53], confirming a tendency of ω to align with the TNTI.

IV. SUMMARY AND CONCLUSIONS

We presented a DNS study of the TNTI in shearless stratified turbulent flows, with a buoyancy jump between two layers. We focus on the question of similarity at small scales in the proximity of the interface of two fluid cases, forced by two distinctly different ways: convective forcing using a constant heat flux versus an agitation resembling an oscillating grid.

We confirmed that in the stratified cases considered here, the common approach to identify the TNTI based on the enstrophy threshold is not reliable, since ω^2 is no longer representative of the viscous processes across the turbulent/nonturbulent boundary alone, but can also contain contributions from internal waves. The latter were caused by the interaction of the turbulence with

a stratified layer which developed due to molecular diffusion. Hence the potential enstrophy Π^2, which is not affected by stratification-related phenomena, needs to be used to define TNTI in both shearless cases, similarly to [19,35]. Based on the analogy between the enstrophy ω^2 and potential enstrophy Π^2 we defined a lengthscale η_Π. Using this lengthscale, the basic TNTI statistics for the two cases collapsed onto each other. Furthermore, the lengthscale clearly distinguished between the turbulent region and the near-TNTI region in the slopes of the profiles of turbulent properties. The near-TNTI region defined by our lengthscale also reflects the fact that the vortical structures realign to the interface within this region (while being randomly oriented in the turbulent core). However, there were also indicators that did not collapse onto one curve, such as Re_ϵ and the turbulent heat flux $\overline{w'b'}$.

In light of the intriguing results for the lengthscale η_Π, it will be crucial to explore the behavior for these flow cases at higher Re_b and also for other canonical flows, such as a stratified wake. Furthermore, it may be interesting to analyze the various terms of the potential-enstrophy equation, to obtain more detailed description of the physical phenomena that influence Π^2, similar to the study of [35]. It is also interesting to test if this scale has presence in the small-scale dynamics of turbulent linearly stratified flows.

ACKNOWLEDGMENTS

[1] C. Bretherton, Entrainment, detrainment and mixing in atmospheric convection, in *The Physics and Parameterization of Moist Atmospheric Convection*, NATO ASI Series (Series C: Mathematical and Physical Sciences), Vol. 505, edited by R. Smith (Springer, Berlin, 1997), pp. 211–230.

[2] M. Holzner and B. Luthi, Laminar Superlayer at the Turbulence Boundary, Phys. Rev. Lett. **106**, 134503 (2011).

[3] T. Watanabe, C. da Silva, Y. Sakai, K. Nagata, and T. Hayase, Lagrangian properties of the entrainment across turbulent/non-turbulent interface layers, Phys. Fluids **28**, 031701 (2016).

[4] S. Corrsin and A. Kistler, Free-stream boundaries of turbulent flows, NACA Technical Report No. TR-1244 (1955), https://ntrs.nasa.gov/search.jsp?R=19930092246#:~:text=Free%2DStream%20Boundaries%20of%20Turbulent%20Flows%20Report%20presents%20the%20results,at%20a%20free%2Dstream%20boundary.

[5] C. B. Da Silva, J. C. R. Hunt, I. Eames, and J. Westerweel, Interfacial layers between regions of different turbulence intensity, Annu. Rev. Fluid Mech. **46**, 567 (2014).

[6] R. Taveira and C. da Silva, Characteristics of the viscous superlayer in shear free turbulence and in planar turbulent jets, Phys. Fluids **26**, 021702 (2014).

[7] J. Westerweel, C. Fukushima, J. M. Pedersen, and J. C. R. Hunt, Mechanics of the Turbulent-Nonturbulent Interface of a Jet, Phys. Rev. Lett. **95**, 174501 (2005).

[8] M. Holzner, A. Liberzon, N. Nikitin, B. Lüthi, W. Kinzelbach, and A. Tsinober, Small-scale aspects of flows in proximity of the turbulent/nonturbulent interface, Phys. Fluids **19**, 071702 (2007).

[9] M. Holzner, A. Liberzon, N. Nikitin, B. Lüthi, W. Kinzelbach, and A. Tsinober, A Lagrangian investigation of the small-scale features of turbulent entrainment through particle tracking and direct numerical simulation, J. Fluid Mech. **598**, 465 (2008).

[10] M. Wolf, B. Lüthi, M. Holzner, D. Krug, W. Kinzelbach, and A. Tsinober, Investigations on the local entrainment velocity in a turbulent jet, Phys. Fluids **24**, 105110 (2012).

[11] C. da Silva and R. Taveira, The thickness of the turbulent/nonturbulent interface is equal to the radius of the large vorticity structures near the edge of the shear layer, Phys. Fluids **22**, 121702 (2010).

[12] A. Attili and F. Bisetti, Statistics and scaling of turbulence in a spatially developing mixing layer at $Re_\lambda = 250$, Phys. Fluids **24**, 035109 (2012).

[13] A. Attili and F. Bisetti, Application of a robust and efficient Lagrangian particle scheme to soot transport in turbulent flames, Comput. Fluids **84**, 164 (2013).

[14] D. Bisset, J. Hunt, and M. Rogers, The turbulent/non-turbulent interface bounding a far wake, J. Fluid Mech. **451**, 383 (2002).

[15] G. Cafiero and J. C. Vassilicos, Nonequilibrium Scaling of the Turbulent-Nonturbulent Interface Speed in Planar Jets, Phys. Rev. Lett. **125**, 174501 (2020).

[16] N. Reuther and C. Kähler, Evaluation of large-scale turbulent/non-turbulent interface detection methods for wall-bounded flows., Exp. Fluids **59**, 121 (2018).

[17] T. Watanabe, X. Zhang, and K. Nagata, Turbulent/non-turbulent interfaces detected in DNS of incompressible turbulent boundary layers, Phys. Fluids **30**, 035102 (2018).

[18] T. Watanabe, Y. Sakai, K. Nagata, Y. Ito, and T. Hayase, Turbulent mixing of passive scalar near turbulent and non-turbulent interface in mixing layers, Phys. Fluids **27**, 085109 (2015).

[19] T. Watanabe, J. J. Riley, S. M. de Bruyn Kops, P. J. Diamessis, and Q. Zhou, Turbulent/non-turbulent interfaces in wakes in stably stratified fluids, J. Fluid Mech. **797**, R1 (2016).

[20] D. Krug, M. Holzner, B. Luthi, M. Wolf, W. Kinzelbach, and A. Tsinober, The turbulent-nonturbulent interface in a inclined dense gravity current, J. Fluid Mech. **765**, 293 (2015).

[21] D. Krug, D. Chung, J. B. Philip, and I. Marusic, Global and local aspects of entrainment in temporal plumes, J. Fluid Mech. **812** (2017).

[22] J. S. Turner, *Buoyancy Effects in Fluids*, Cambridge Monographs on Mechanics (Cambridge University Press, Cambridge, UK, 1973).

[23] G. Csanady, Turbulent diffusion in a stratified fluid, J. Atmos. Sci. **21**, 439 (1964).

[24] J. S. Turner, The influence of molecular diffusivity on turbulent entrainment across a density interface, J. Fluid Mech. **33**, 639 (1968).

[25] H. Fernando, Turbulent mixing across density interfaces: A review of laboratory experiments and their oceanographic implications, in *Proceedings of the Aha Hulikoa Fifth Hawaiian Winter Workshop* (U.S. Office of Naval Research, 1989), pp. 205–218.

[26] E. L. G. Kit, E. J. Strang, and H. J. S. Fernando, Measurement of turbulence near shear-free density interfaces, J. Fluid Mech. **334**, 293 (1997).

[27] H. E. Gilreath and A. Brandt, Experiments on the generation of internal waves in a stratified fluid, AIAA J. **23**, 693 (1985).

[28] P. Bonneton, J. M. Chomaz, and E. J. Hopfinger, Internal waves produced by the turbulent wake of a sphere moving horizontally in a stratified fluid, J. Fluid Mech. **254**, 23 (1993).

[29] A. M. Abdilghanie and P. J. Diamessis, The internal gravity wave field emitted by a stably stratified turbulent wake, J. Fluid Mech. **720**, 104 (2013).

[30] K. Dohan and B. Sutherland, Internal waves generated from a turbulent mixed region, Phys. Fluids **15**, 488 (2003).

[31] A. Maffioli, P. A. Davidson, S. B. Dalziel, and N. Swaminathan, The evolution of a stratified turbulent cloud, J. Fluid Mech. **739**, 229 (2014).

[32] J. Lighthill, Internal waves and related initial-value problems, Dyn. Atmos. Oceans **23**, 3 (1996).

[33] J. J. Riley and M.-P. Lelong, Fluid motions in the presence of strong stable stratification, Annu. Rev. Fluid Mech. **32**, 613 (2000).

[34] K. Fodor and J. P. Mellado, New insights into wind shear effects on entrainment in convective boundary layers using conditional analysis, J. Atmos. Sci. **77**, 3227 (2020).

[35] T. Watanabe, J. J. Riley, K. Nagata, R. Onishi, and K. Matsuda, A localized turbulent mixing layer in a uniformly stratified environment, J. Fluid Mech. **849**, 245 (2018).

[36] M. van Reeuwijk, H. J. J. Jonker, and K. Hanjalić, Wind and boundary layers in Rayleigh-Bénard convection. I. Analysis and modeling, Phys. Rev. E **77**, 036311 (2008).

[37] M. van Reeuwijk, H. J. J. Jonker, and K. Hanjalić, Wind and boundary layers in Rayleigh-Bénard convection. II. Boundary layer character and scaling, Phys. Rev. E **77**, 036312 (2008).

[38] R. W. C. P. Verstappen and A. E. P. Veldman, Symmetry-preserving discretization of turbulent flow, J. Comput. Phys. **187**, 343 (2003).

[39] F. S. Godeferd and L. Lollini, Direct numerical simulations of turbulence with confinement and rotation, J. Fluid Mech. **393**, 257 (1999).

[40] G. Khujadze and M. Oberlack, Turbulent diffusion: Direct numerical simulation, PAMM **9**, 451 (2009).

[41] Y. Morinishi, Z. Liu, T. Nagao, and S. Tamano, Experimental and numerical study of oscillating grid turbulence subjected to system rotation, in *Proceedings of the 14th European Turbulence International Symposium of Turbulence Conference* (Lyon, France, 2013), http://etc14.ens-lyon.fr/etc-14-proceedings/accepted-talks/.

[42] R. R. Long, Theory of turbulence in a homogeneous fluid induced by an oscillating grid, Phys. Fluids **21**, 1887 (1978).

[43] L. Verso, M. van Reeuwijk, and A. Liberzon, Steady state model and experiment for an oscillating grid turbulent two-layer stratified flow, Phys. Rev. Fluids **2**, 104605 (2017).

[44] H. J. Fernando and R. R. Long, Experiments on steady buoyancy transfer through turbulent fluid layers separated by density interfaces, Dyn. Atmos. Oceans **12**, 233 (1988).

[45] J. Deardorff, Convective velocity and temperature scales for the unstable planetary boundary layer and for Rayleigh convection, J. Atmos. Sci. **27**, 1211 (1970).

[46] H. Jonker, M. Van Reeuwijk, P. Sullivan, and E. Patton, Interfacial layers in clear and cloudy atmospheric boundary layers, in *Turbulence, Heat and Mass Transfer 7* (Begel House, Palermo, Italy, 2012).

[47] R. R. Long, A theory of mixing in a stably stratified fluid., J. Fluid Mech. **84**, 113 (1978).

[48] R. R. Taveira, J. S. Diogo, D. C. Lopes, and C. B. da Silva, Lagrangian statistics across the turbulent-nonturbulent interface in a turbulent plane jet, Phys. Rev. E **88**, 043001 (2013).

[49] S. A. Thorpe, Layers and internal waves in uniformly stratified fluids stirred by vertical grids, J. Fluid Mech. **793**, 380 (2016).

[50] G. Taylor, Statistical theory of turbulence, Proc. R. Soc. London A **151**, 421 (1935).

[51] R. A. Antonia, J. Kim, and L. W. B. Browne, Some characteristics of small-scale turbulence in a turbulent duct flow, J. Fluid Mech. **233**, 369 (1991).

[52] R. Godoy-Diana, J. Chomaz, and P. Billant, Vertical length scale selection for pancake vortices in strongly stratified viscous fluids, J. Fluid Mech. **504**, 229 (2004).

[53] C. da Silva and R. dos Reis, The role of coherent vortices near the turbulent/non-turbulent interface in a planar jet, Philos. Trans. R. Soc. London A **369**, 738 (2011).

[54] H. Helmholtz, über integrale der hydrodynamischen gleichungen, welche den wirbelbewegungen entsprechen, Journal für die reine und Angewandte Mathematik **55**, 25 (1858).